Electrocatalysis
https://doi.org/10.1007/s12678-022-00798-4

ORIGINAL RESEARCH

Development of Unsupported Ru and Ni Based Oxides with Enhanced Performance for the Oxygen Evolution Reaction in Acidic Media

Franschke A. Soudens[1] · Simoné Karels[1] · Cecil Felix[1] · Sivakumar Pasupathi[1]

Accepted: 29 November 2022
© The Author(s), under exclusive licence to Springer Science+Business Media, LLC, part of Springer Nature 2023

Abstract

The high cost of catalyst materials suitable for the oxygen evolution reaction (OER) in polymer electrolyte membrane water electrolyzers (PEMWE) is still a major hurdle that needs overcoming before commercial PEMWE can have a meaningful impact as a technology in the hydrogen economy. Metal oxides based on precious metals are currently still the most reliable and most used materials as catalysts in PEMWE; however, alternative or modified materials are desirable to help reduce the cost associated with the catalyst component. In this study, we report on binary metal oxide catalysts based on Ru and Ni. Ni-based electrodes are typically used in alkaline water electrolyzers due to their high performance, robustness and low cost; however, Ni and NiO electrodes do not show promising performance in acidic environments due to corrosion. By combining NiO with acid stable RuO_2, we have demonstrated that the performance of the RuO_2 catalyst can be improved and due to the lower cost of Ni, the cost of the catalyst can ultimately be reduced. The Ni addition was limited to 10 mol% to achieve improved OER performance followed by noticeable performance degradation as the Ni composition was increased. The metal oxide catalysts were synthesized via a modified Adams fusion method that produced nano-sized catalysts with superior performance compared to a state-of-art commercial RuO_2 catalyst. Physical characterizations were performed via high-resolution transmission electron microscopy, X-ray diffraction, energy dispersive X-ray, and Brunauer Emmett Teller analyses. OER performances were evaluated via cyclic voltammetry, linear sweep voltammetry, chronopotentiometry, and chronoamperometry analyses.

Keywords Ruthenium-nickel oxide · Oxygen evolution reaction · Modified Adams fusion method · Polymer electrolyte membrane water electrolyser

Introduction

In 2019, it was estimated that the annual energy related CO_2 emissions was 33.3 metric gigatons due to our global dependence on fossil fuels [1]. The CO_2 emissions plummeted somewhat in 2020 due to restrictions on movement and lower industrial activity; however, CO_2 emissions are expected to increase again with the opening up of economies. Multi sustainability agendas and initiatives are emerging in response to environmental challenges such as climate change, resource depletion, and pollution [2]. Hydrogen as a clean, reliable, and sustainable energy source is considered by many, both researchers and policy makers, to be a key player in revolutionizing our energy system and for the decarbonisation of the various energy sectors [1, 3, 4]. Currently about 96% of hydrogen is produced from fossil fuel raw materials [5], while only 4% is produced through the electrolysis of water due to its higher cost [6]. Green hydrogen, derived from renewable energy, is of particular importance and the electrolysis of water has been identified as a key production technology. The polymer electrolyte membrane water electrolyser (PEMWE) is a low temperature technology that is especially suitable for the intermittent energy profile of photovoltaic solar systems. However, because of the acidic environment and high over-potential at the anode due to sluggish electrode kinetics [7], the oxygen evolution reaction (OER) demands highly stable materials, typically in the form of expensive precious metals. Therefore, the cost reduction of the expensive precious metals required for efficient PEMWE remains a major hurdle for

✉ Franschke A. Soudens
fsoudens@gmail.com

[1] South African Institute for Advance Materials Chemistry (SAIAMC), University of the Western Cape, Robert Sobukwe Road, Bellville, Cape Town 7535, South Africa

Published online: 02 January 2023

significant market penetration. Precious metals are known to be the most stable and active toward the OER although alternative non-precious metal materials are also being investigated [8]. RuO_2 is known to be the most active catalyst for the OER in acidic media; however, it lacks the higher stability and durability of IrO_2 due to the over-oxidation of Ru to the soluble RuO_4 moiety [9]. Numerous studies have focused on improving the stability of the RuO_2 catalyst without compromising its excellent catalytic activity [10]. To achieve a high performance RuO_2 catalyst, some studies have investigated various synthesis methods as well as the use of catalyst supports [11–16]. Additionally, binary and ternary metal oxides based on RuO_2 have been developed, where metals such as Mo, Sn, Cu, Ir, Cr, Pt, Ni, and Pd have been added, to enhance the performance of the RuO_2 catalyst through synergistic effects [17–23].

Tailoring the electronic structure or tuning the surface structure and interfaces of a substance can lead to the production of unique materials. Additionally, catalytic performance is highly dependent on the catalyst morphology, size, porosity, and surface microstructure. Ni has shown great synergistic catalytic effects resulting in improved surface adsorption properties leading to enhanced catalytic performance. Ni is also studied due to its low cost, abundance, high corrosion resistance, and high electrical conductivity [7]. Although Ni has been mostly studied as a catalyst for the OER in alkaline media, the addition of Ni to a more acid stable metal has been shown to improve the stability of Ni in acidic media [24]. In this study, the high activity of RuO_2 was combined with the low cost NiO to produce binary metal oxide catalysts that exhibited improved OER catalytic performance at a reduced cost. A modified Adams fusion method, which is known to directly produce nano-sized metal oxides, was used to synthesize the catalysts. To the best of the authors' knowledge, an unsupported RuNiOx synthesized via the Adams fusion method for the OER has not been reported in the literature. The metal oxides were characterized using high-resolution transmission electron microscopy (HRTEM), X-ray diffraction (XRD), energy-dispersive X-ray (EDX), and Brunauer–Emmett–Teller (BET) analysis. The metal oxide catalysts were evaluated ex situ via cyclic voltammetry (CV), linear sweep voltammetry (LSV), chronopotentiometry (CP), and chronoamperometry (CA).

Experimental Method

Electrocatalyst Synthesis

$RuCl_3$ (SA Precious Metals) and $NiCl_2$ (Sigma-Aldrich) were used as precursors to synthesize the RuO_2, NiO, and $Ru_xNi_{1-x}O_x$ catalysts. An amount of 0.36 g precursor was dissolved in 10 ml isopropanol (Sigma-Aldrich) and magnetically stirred for 30 min. Finely ground $NaNO_3$ (Alfa Aesar) was added to the solution, which was then stirred for an additional 30 min. For the binary metal oxide catalyst, the composition of Ni was varied in the range of 5–25 mol% to Ru. Excess solvent was evaporated on a hot plate followed by further drying in an oven for 30 min at 90 °C. The dried catalyst precursor/$NaNO_3$ mixture was then reacted in a furnace for 2 h at 350 °C. No additional calcining step was performed. The obtained metal oxide was cooled, rinsed, and filtered with 1.5 L of ultrapure water (Milli Q) to remove the unreacted $NaNO_3$. The final step was to dry the metal oxide in an oven for 4 h at 85 °C then cool down overnight inside the oven. A commercial RuO_2 electrocatalyst (Sigma-Aldrich), labelled comm RuO_2 on all graphs, was used for comparison purposes. The prefix "in-house" was added to the synthesized RuO_2 to distinguish between the commercial and synthesized RuO_2 catalysts.

Preparation of the Working Electrode

A Metrohm rotating disc electrode (RDE) setup and glassy carbon (GC) electrode with 0.1963 cm^2 working area was used for electrochemical experiments. The GC electrode was cleaned, then polished using 0.05 µm deagglomerated alumina paste (Buehler) before each use, followed by ultrasonication in ultrapure water for 15 min. The GC electrode was dried on the RDE using a speed of 2500 rpm for 15 min. The catalyst ink was prepared by combining 8 mg of the electrocatalyst, 50 µL 5 wt % Nafion® solution (Alfa Aesar) and 1950 µL UP water and ultrasonicating for 20 min. A micropipette was used to drop 30 µL of the catalyst ink onto the GC electrode. The working electrode was covered with a glass beaker and dried for 24 h at ambient conditions. A calculated catalyst loading of 0.6 mg cm^{-2} was obtained.

Physical Characterization

Physical phases and structures of the electrocatalysts were characterized by X-ray diffraction (XRD) employing the Bruker AXS D8 Advance diffractometer using Cu K_α radiation ($\lambda = 1.5406$ Å) operating at 40 kV and 40 mA. The RuO_2 standard (JCP-No 00–40-1290) and NiO standard (JCP-No 00–047-1049) were used for peak allocation. Transmission electron micrographs (TEM) were obtained using a FEI/Tecnai T20 operating at 200 kV. Brunuaer Emmett Teller (BET) surface area analysis was obtained using the Micromeritics 3 Flex surface characterization analyzer. Energy-dispersive X-ray (EDX) compositional analysis was performed using the Carl Zeiss Auriga HR-SEM.

Electrochemical Characterization

Electrochemical analyses were performed ex-situ in a three-electrode setup at 25 °C and atmospheric pressure. Cell

temperature was maintained using a circulating water bath (SMC). The working electrode (described in 2.2), a 3 M Ag/AgCl reference electrode (Metrohm), a 1 cm^2 Pt sheet counter electrode (Metrohm), and a 0.5 M H_2SO_4 electrolyte solution were used. The geometric area of the Pt counter electrode was 5 times larger than the working electrode. All potentials in this work are reported versus the reversible hydrogen electrode (RHE) by adding 0.21 V to the measured potentials. The current densities reported are based on the geometric surface area of the glassy carbon working electrode by converting the surface area of the working electrode to 1 cm^2 through dividing the measured current by the geometric surface area of the glassy carbon electrode. The Autolab potentiostat PGSTAT302N (Metrohm) was used for all electrochemical analyses. The electrolyte solution was purged with N_2 for 15 min before performing electrochemical measurements. The electrodes were activated by CV cycling between 0 V and + 1.4 V vs. RHE at a 200 mV s^{-1} potential scan rate for 50 cycles before conducting any characterization.

Results and Discussion

Physical Characterization

Figure 1 shows the XRD analysis of commercial RuO_2, in-house RuO_2 and NiO. The XRD patterns for commercial and in-house RuO_2 are very similar and fit well with the reference patterns for crystalline RuO_2 (JCP-No 00–40-1290). Both RuO_2 samples are crystalline with a rutile type oxide structure. There is no metallic Ru present in both samples. The XRD pattern for NiO shows a bunsenite structure and fits well with the reference pattern for NiO (JCP-No 00–047-1049). The XRD peaks for NiO are sharp indicating a highly crystalline material.

The XRD analysis of the $Ru_xNi_{1-x}O_x$ catalysts is shown in Fig. 2. The reference patterns of RuO_2 and NiO were used to assign the peaks of the binary metal oxides. The structures of the $Ru_xNi_{1-x}O_x$ catalysts seem to resemble a rutile type oxide structure similar to RuO_2. As the composition of the Ni component was increased to 10 mol %, an increase in crystallinity was observed. However, as the composition increased above 10 mol %, the material became less crystalline and the dominant facets associated with RuO_2 also decreased. At 25 mol % Ni, small peaks of NiO emerged and some of the facets of RuO_2 completely disappeared. It seems that the $Ru_xNi_{1-x}O_x$ catalysts did not form solid solution phases as there were no merged peaks.

The average crystallite sizes for the samples were calculated from the (101) facet using the *Scherrer* formula (Eq. (1)):

$$D = {}^{0.9\lambda}/_{\beta cos\theta} \quad (1)$$

where d = average crystallite/particle size, 0.9 = shape factor, λ = wavelength of x-ray, β = peak width at half peak height in radians, θ = *Bragg* angle. Estimated average crystallite sizes are tabulated in Table 1.

The interplanar spacings were calculated using Bragg's law (Eq. (2)) and tabulated in Table 1.

$$n\lambda = 2dsin\theta \quad (2)$$

where, n is the order number, λ is the wavelength (1.541 Å for Cu-K_α radiation), d is the basal spacing (Å) and θ is the diffraction angle (°). XRD analysis revealed that the more crystalline the samples were, the larger the estimated crystallite sizes. NiO was observed to crystallize to a higher degree than RuO_2 at 350 °C however, when combined with RuO_2, the NiO component did not promote the crystallization of the RuO_2 component. The opposite effect, based on the estimated crystallite sizes, was observed. As the Ni component was increased, there was an initial increase in crystallization up to 10 mol %, thereafter crystallization was suppressed resulting in even smaller crystallite sizes. It is possible that when the Ni component was increased beyond 10 mol%, the rutile structure of RuO_2 broke down into an amorphous phase with smaller sizes. It is known that the increase in crystallite size is associated with a decrease in electrochemical surface area of the catalysts [25]. There is still no reliable established method for the determination of the electrochemical surface area of metal oxides, therefore BET surface area analysis was instead performed. A decrease in surface area for the more crystalline samples was observed from BET analysis. A summary of XRD and BET surface area analyses is given in Table 1. The trend in BET surface areas was in agreement with estimated crystallite sizes of determined from XRD.

Figure 3 shows the TEM images for the commercial RuO_2, in-house RuO_2 and NiO samples with the corresponding selective area electron diffraction (SAED) patterns.

The commercial RuO_2 catalyst exhibited larger spherical crystals of 25.3 nm average size. The in-house RuO_2 catalyst exhibited smaller cuboid shaped crystals of 5.1 nm average size, whereas the NiO consisted of spherical and cuboid shaped structures averaging about 43.1 nm. The trend in average sizes obtained with HRTEM was in agreement with the estimated sizes obtained with XRD. Figure 4 shows the HRTEM images for the $Ru_xNi_{1-x}O_x$ catalysts with the corresponding SAED patterns. The measured average crystallite sizes for $Ru_{0.95}Ni_{0.05}O_x$, $Ru_{0.9}Ni_{0.1}O_x$, $Ru_{0.85}Ni_{0.15}O_x$, and $Ru_{0.75}Ni_{0.25}O_x$ were 5.7 nm, 6.8 nm, 5.3 nm and 4.8 nm, respectively. The SAED patterns of the in-house RuO_2 and the $Ru_xNi_{1-x}O_x$ catalyst revealed polycrystalline materials, while the scattered patterns for commercial RuO_2 and NiO are consistent with single or multi crystal materials.

The results of EDX analysis are tabulated in Table 2. The in-house RuO_2 catalyst did not contain any impurities or

chloride residues from the precursor whereas the commercial RuO_2 catalyst contained some trace metals. The NiO contained some Al impurity, and chloride from the precursor salt. Based on the EDX analysis, the following chemical compositions were determined; $Ru_{0.97}Ni_{0.3}O_x$, $Ru_{0.89}Ni_{011}O_x$, $Ru_{0.84}Ni_{0.16}O_x$ and $Ru_{0.77}Ni_{0.23}O_x$. The results are in close agreement with the target compositions.

Electrochemical Characterization

Figure 5 shows the CV of the commercial RuO_2, in-house RuO_2 and NiO samples. All CV experiments were performed at a potential scan rate of 20 mV s^{-1} in a potential window of 0 V and 1.4 V vs the RHE.

The in-house RuO_2 catalyst displayed significantly higher current densities compared to the commercial RuO_2 and NiO. The CVs of the commercial RuO_2 and NiO were magnified and displayed separately for better observation. In-house RuO_2 exhibited the expected two redox couples of RuO_2. At about 0.6 V the Ru(III)/Ru(IV) redox couple is observed, and at about 1.2 V the Ru(IV)/Ru(V) redox couple is observed. The peak anodic current densities for the Ru(III)/Ru(IV) and Ru(IV)/Ru(V) redox transitions were 2.6 mA cm^{-2} and 3 mA cm^{-2}, respectively. The peak cathodic current densities of the Ru(V)/Ru(IV) and Ru(IV)/Ru(III) transitions were – 2.6 mA cm^{-2} and – 1.6 mA cm^{-2}, respectively. The CV for the commercial RuO_2 shows only the Ru(III)/Ru(IV) redox couple. The peak anodic current density, occurring at 0.61 V was 0.2 mA cm^{-2}, while the peak cathodic current density, occurring at 0.54 V was – 0.1 mA cm^{-2}. The two redox transitions for RuO_2 can be illustrated by Eqs. (3) and (4).

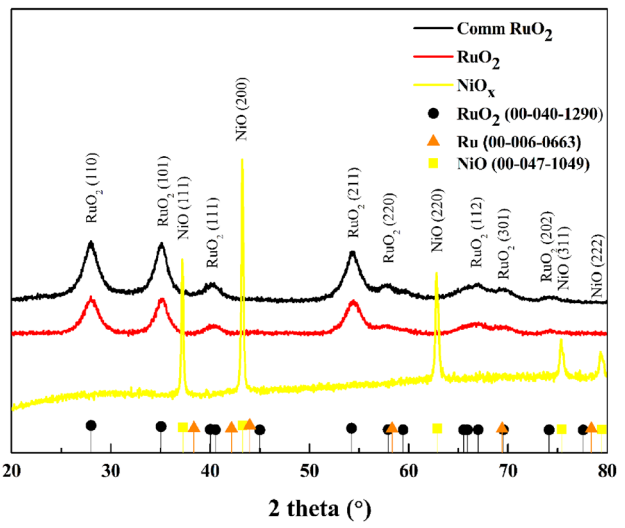

Fig. 1 X-ray diffraction patterns of the commercial RuO_2, in-house RuO_2 and NiO

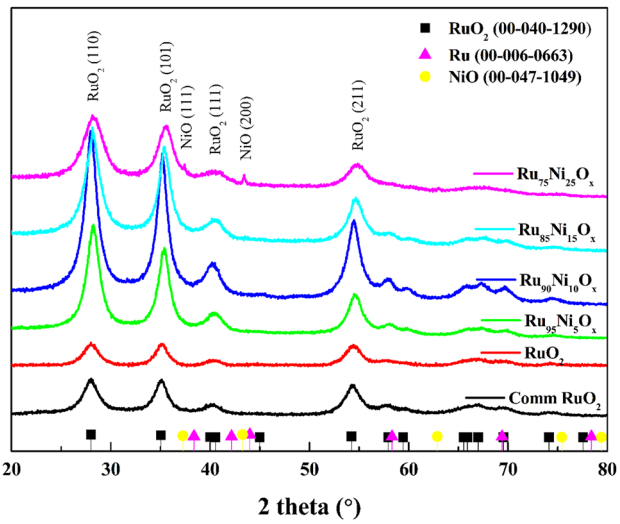

Fig. 2 X-ray diffraction patterns of $Ru_{1-x}Ni_xO_x$ compared to the in-house RuO_2 and commercial RuO_2

$$2RuO_2 + 2H^+ + 2e^- \rightleftharpoons Ru_3O_2 + H_2O \quad (3)$$

$$\frac{1}{2}RuO_5 + 3H^+ + e^- \rightleftharpoons Ru(OH)_2{}^{2+} + \frac{1}{2}H_2O \quad (4)$$

The hydrogen sorption region occurs at potentials lower than 0.4 V, where Ru-OH intermediates are formed and a mixture of Ru(I) to Ru(III) is likely to be present. Both the in-house RuO_2 and the commercial RuO_2 catalysts exhibited the hydrogen sorption negative tail approaching 0 V. For the NiO catalyst, a single redox couple corresponding to Ni(II)/Ni(III), was observed at about 0.6 V. The peak anodic current density, occurring at 0.6 V, was 0.07 mA cm^{-2} while the peak cathodic current density, occurring at 0.5 V, was – 0.08 mA cm^{-2}. The negative tail observed below 0.2 V could be ascribed to hydrogen adsorption. Figure 6 shows the CVs of the in-house RuO_2 and the binary metal oxide catalysts.

The CVs of the $Ru_xNi_{1-x}O_x$ catalysts resemble that of the in-house RuO_2. As the Ni composition was increased, the current density of the two redox couples was observed

Table 1 Summary of XRD and BET analyses

Sample	XRD crystallite size (nm)	Interplanar d-spacing (Å)	BET surface area (m^2/g)
Comm-RuO_2	22.38	1.76	13.08
RuO_2	4.18	1.91	114.78
NiO	33.34	1.69	5.67
$Ru_{0.95}Ni_{0.05}O_x$	5.19	1.78	133.72
$Ru_{0.9}Ni_{0.1}O_x$	5.74	1.71	128.93
$Ru_{0.85}Ni_{0.15}O_x$	4.82	1.82	132.33
$Ru_{0.75}Ni_{0.25}O_x$	3.27	2.00	149.95

to decrease. Thus, the two redox couples observed at 0.6 V and 1.2 V can be ascribed to Ru(III)/Ru(IV) and Ru(V)/Ru(VI), respectively, since Ni does not contribute significantly to the observed current density. The negative tail related to hydrogen adsorption was also present, which decreased as the Ru composition was decreased. Figure 7 shows the LSV analysis of both single metal oxide catalysts and binary metal oxide catalysts. The in-house RuO_2 catalyst shows notably better activity compared to the commercial RuO_2 and NiO catalysts. The NiO catalyst showed poor OER activity and very low current density. The poor performance of NiO in acidic media was also observed by Li et al. [24], which they ascribed to rapid dissolution, even at a much lower current density of 1 mA cm^{-2}. Most metal oxides exhibit amphoterism in aqueous solution. The following acid–base equilibrium

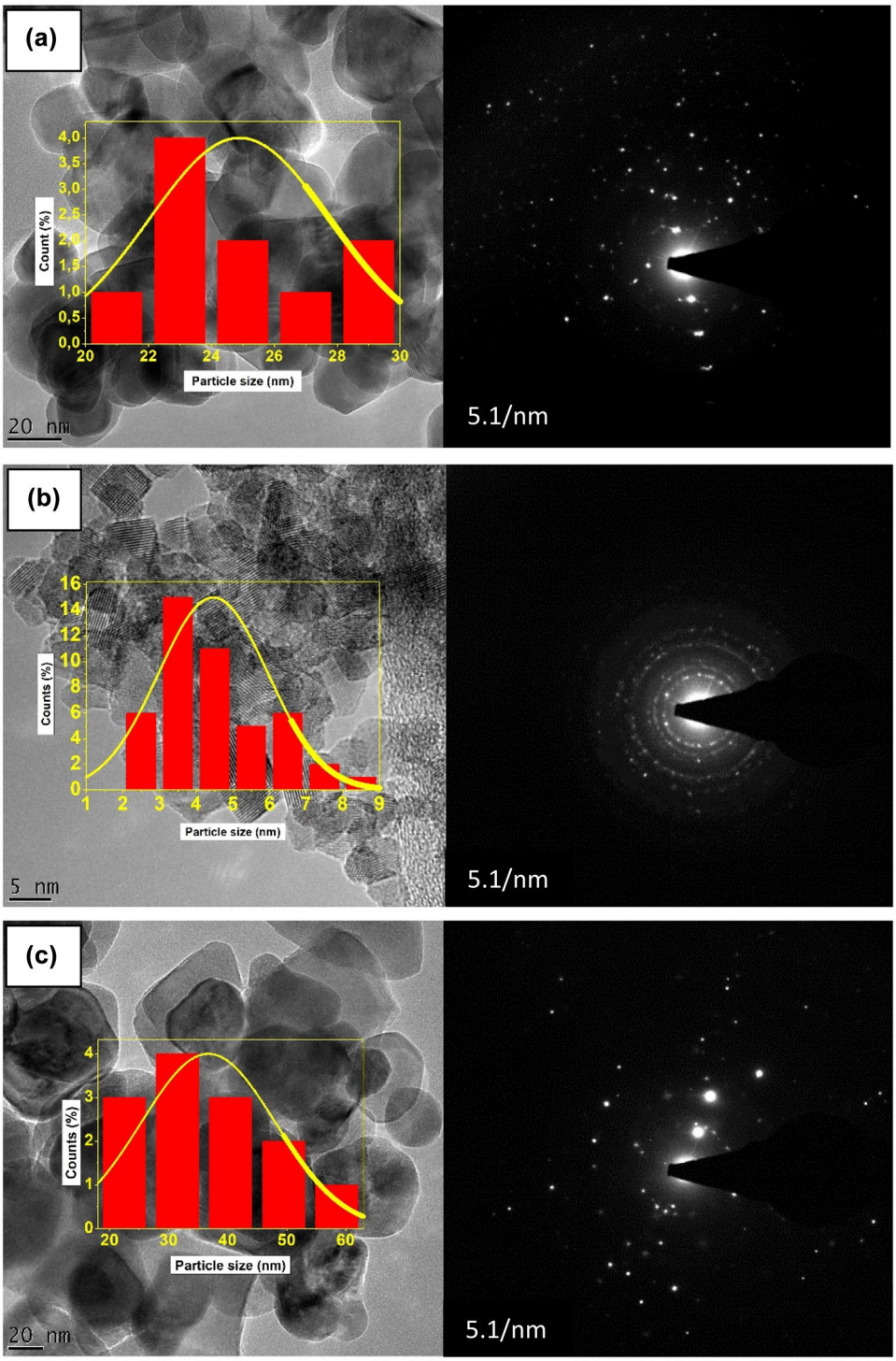

Fig. 3 Transmission electron micrographs and selective area electron diffraction images of (**a**) commercial RuO_2, (**b**) in-house RuO_2, and (**c**) NiO

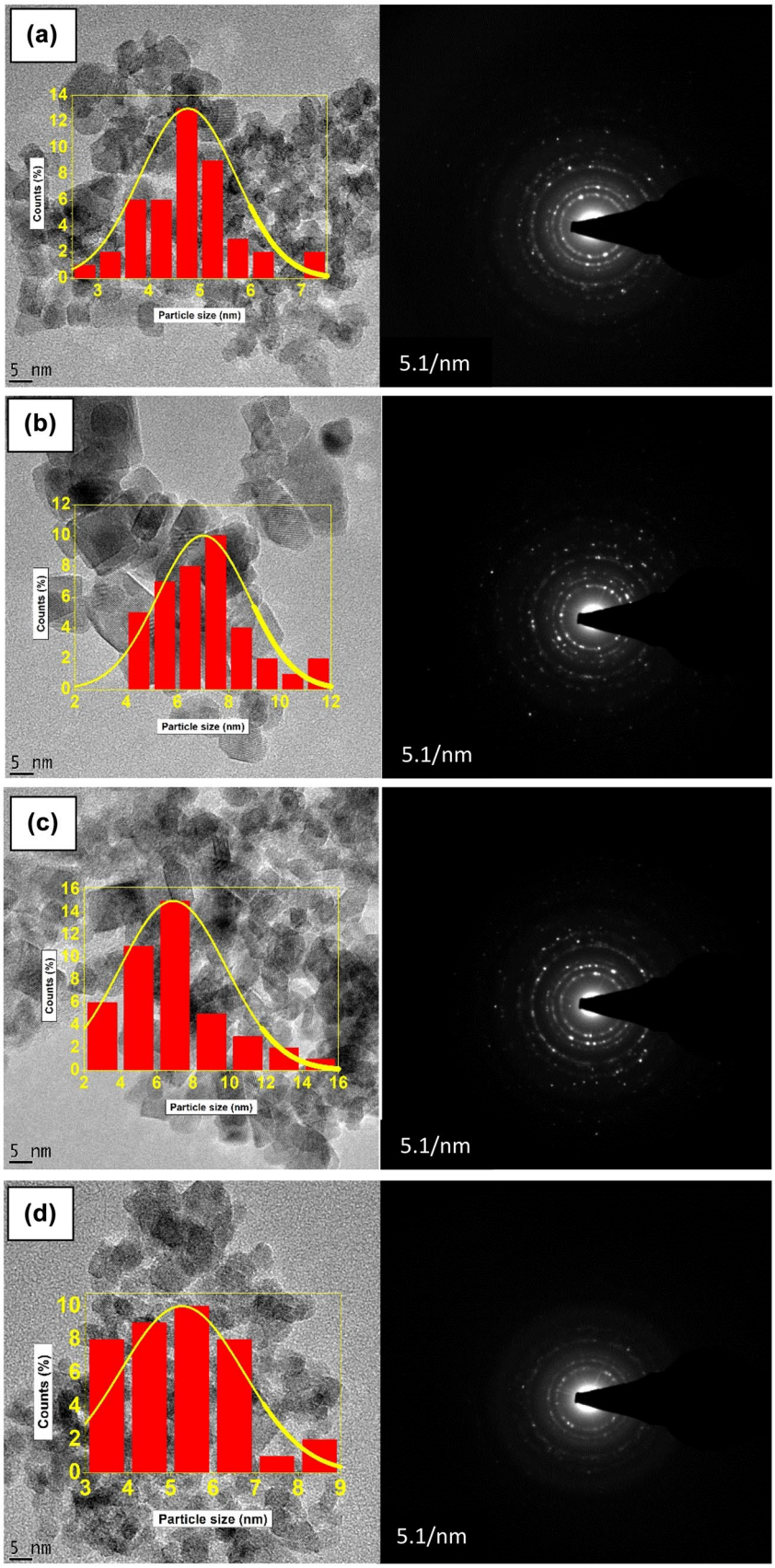

Fig. 4 Transmission electron micrographs and selective area electron diffraction images of (**a**) $Ru_{0.95}Ni_{0.05}O_x$, (**b**) $Ru_{0.9}Ni_{0.1}O_x$, (**c**) $Ru_{0.85}Ni_{0.15}O_x$, and (**d**) $Ru_{0.75}Ni_{0.25}O_x$

Table 2 EDX analysis of commercial and in-house catalysts

Sample	Element	Atomic %
Comm RuO_2	O	62.23
	Ru	36.1
	Na	0.74
	Zn	0.93
RuO_2	O	60
	Ru	40
NiO	O	37.76
	Ni	61.34
	Al	0.45
	Cl	0.45
$Ru_{0.95}Ni_{0.05}O_x$	O	69.38
	Ru	29.62
	Ni	1
$Ru_{0.9}Ni_{0.1}O_x$	O	63.4
	Ru	32.72
	Ni	3.89
$Ru_{0.85}Ni_{0.15}O_x$	O	67.61
	Ru	27.32
	Ni	5.08
$Ru_{0.75}Ni_{0.25}O_x$	O	64.97
	Ru	27.01
	Ni	8.02

(Eq. (5)) shows the reaction of hydroxyl groups on the surface of NiO.

$$NiO^- \underset{-H^+}{\overset{+H^+}{\rightleftarrows}} NiOH \underset{-H^+}{\overset{+H^+}{\rightleftarrows}} NiOH_2^+ \quad (5)$$

As the pH decreases, the equilibrium shifts to the right and the less active NiO^- remains, which could explain the low current density obtained. The binary $Ru_xNi_{1-x}O_x$ catalysts exhibited good activities with $Ru_{0.9}Ni_{0.1}O_x$ achieving the highest current density at 1.8 V. The inset shows the Tafel slopes for the commercial IrO_2, in-house RuO_2 and $Ru_xNi_{1-x}O_x$ catalysts determined between 5 and 50 $mAcm^{-2}$. Table 3 summarizes the onset OER potentials, overpotentials at 10 $mAcm^{-2}$ and the Tafel slopes of the metal oxide catalysts.

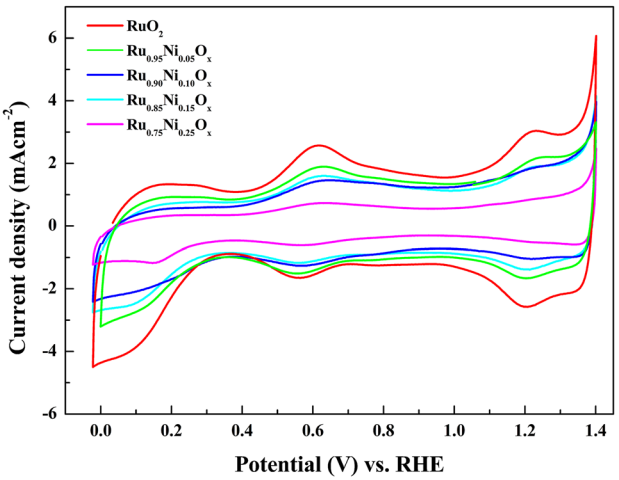

Fig. 6 Cyclic voltammograms of the $Ru_xNi_{1-x}O_x$ catalysts compared to in-house RuO_2 performed at 20 mV s^{-1} in 0.5 M H_2SO_4 at 25 °C and atmospheric pressure

Figure 8 shows the CP analysis of the commercial RuO_2, in-house RuO_2 and $Ru_{1-x}Ni_xO_x$ catalysts. The tests were performed at 10 mA cm^{-2} using RDE speed of 1600 rpm. The tests were performed until a potential limit of 1.8 V, or a time limit of 110 h was reached. NiO was excluded as it did not

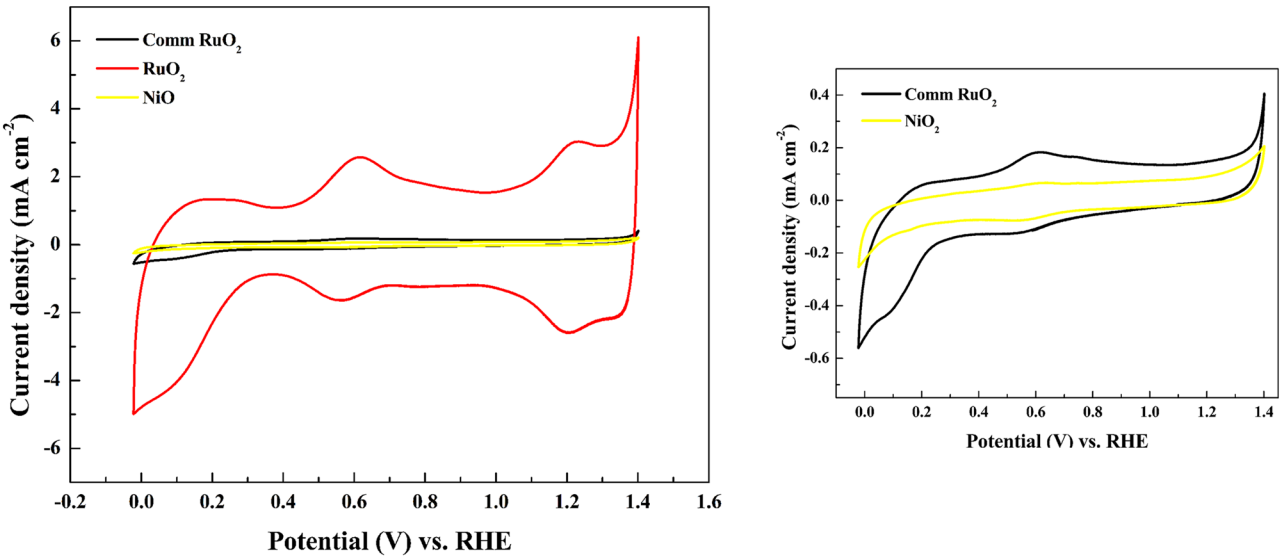

Fig. 5 Cyclic voltammograms of the commercial RuO_2, in-house RuO_2 and NiO measured at 20 mV s^{-1} in 0.5 M H_2SO_4 at 25 °C and atmospheric pressure

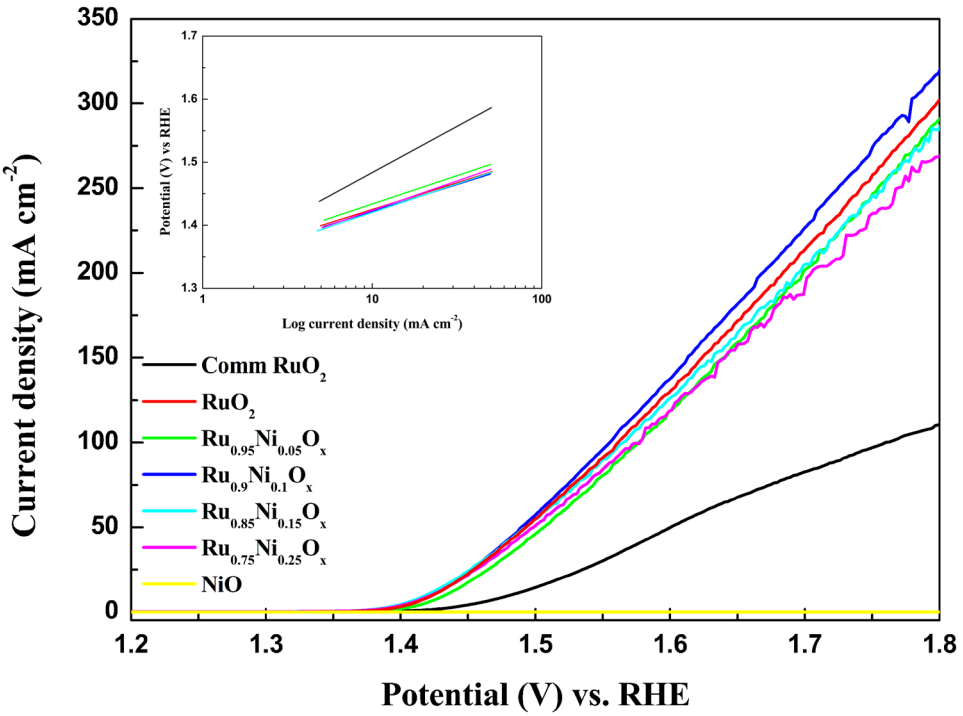

Fig. 7 Linear sweep voltammograms of all the catalysts performed at 2 mVs^{-1} in 0.5 M H_2SO_4 at 25 °C and atmospheric pressure. The Tafel slopes of Ru based metal oxides are provided in the inset

show any performance at the applied current density due to instability. The in-house RuO_2 catalyst showed stability for about 49 h before reaching 1.8 V. The result for the in-house RuO_2 catalyst is similar to what have been reported in literature [9]. The commercial RuO_2 catalyst was only stable for about 7 h before reaching the potential limit of 1.8 V. The low stability could be due to the larger crystallite sizes and smaller surface area. Furthermore, dissolution of RuO_2 is an expected reason for the decay in stability with time. At potentials above 1.4 V, dissolution of RuO_2 to RuO_4, a corrosion product that forms during the OER, occurs [26]. The improved stability of the in-house RuO_2 catalyst could be attributed to the smaller crystallite size and larger surface area compared to the commercial RuO_2 catalyst. Larger surface areas lead to more accessibility to the catalyst active sites. Thus, the applied current density could be maintained at a lower voltage for longer durations. The synthesis method therefore plays a key role in the performance of the catalyst formed.

The addition of 5 and 10 mol% Ni to RuO_2 resulted in an improved stability compared to RuO_2. $Ru_{0.9}Ni_{0.1}O_x$ remained stable for 110 h (experimental time limit) and $Ru_{0.95}Ni_{0.05}O_x$ was stable for 55 h while RuO_2 was stable for 48 h. It is suggested that the NiO acts as a sacrificial component which delays the dissolution of RuO_2 [27]. The addition of 15 and 25 mol% Ni to RuO_2 resulted in a rapid decrease in stability. A possible explanation for this observation is that, as the NiO composition was increased, the less active and less stable Ni component covered the RuO_2 component thereby blocking access to the RuO_2 active sites for electrochemical reactions. Furthermore, NiO is oxidized to the less active NiO_2 which results in the formation of a passivation layer on the electrode which in turn would lead to an increase in ohmic resistance. NiO_2 is presumed to suppress the catalytic activity of RuO_2 [28]. The LSV analysis demonstrated that the pure NiO catalyst exhibited poor performance toward the OER in acidic media. Thus, the rapid corrosion of the

Table 3 Summary of LSV electrochemical properties

Sample	OER onset potential (V) at 1 $mAcm^{-2}$	Overpotential at 10 $mAcm^{-2}$ (V)	Tafel slopes 5 – 50 $mAcm^{-2}$ (mV dec^{-1})
Comm-RuO_2	1.41	0.252	147
RuO_2	1.38	0.193	85
$Ru_{0.95}Ni_{0.05}O_x$	1.39	0.203	90
$Ru_{0.9}Ni_{0.1}O_x$	1.37	0.189	85
$Ru_{0.85}Ni_{0.15}O_x$	1.37	0.193	90
$Ru_{0.75}Ni_{0.25}O_x$	1.37	0.193	93

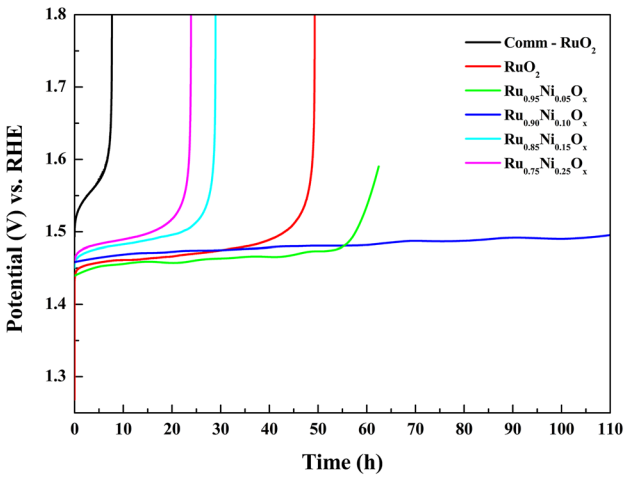

Fig. 8 Chronopotentiometry curves of the commercial RuO_2, in-house RuO_2 and the $Ru_xNi_{1-x}O_x$ catalysts performed at 10 $mAcm^{-2}$ in 0.5 M H_2SO_4 at 25 °C and atmospheric pressure

NiO component, especially at higher compositions, were detrimental to the performance of the $Ru_xNi_{1-x}O_x$ catalysts. Particle size did not appear to impact the stability of the $Ru_xNi_{1-x}O_x$ catalysts since at higher NiO compositions, smaller crystallite sizes were observed.

Figure 9 a–d shows the CA analysis of the commercial RuO_2, in-house RuO_2 and $Ru_xNi_{1-x}O_x$ catalysts. NiO was excluded due to its poor OER performance. CA analysis was performed at 1.5 V, 1.6 V, 1.7 V, and 1.8 V vs. the RHE for 30 min at each potential. The RDE speed was 1600 rpm. Compared to the in-house RuO_2 and $Ru_xNi_{1-x}O_x$ catalysts, the commercial RuO_2 showed significantly lower performance. Lower current densities were observed for all samples compared to the current densities observed during LSV at the respective potentials. This could be due to how the potentiostat/galvanostat performs the analysis and also the short duration of the LSV analysis. $Ru_{0.9}Ni_{0.1}O_x$ showed the highest activity across all

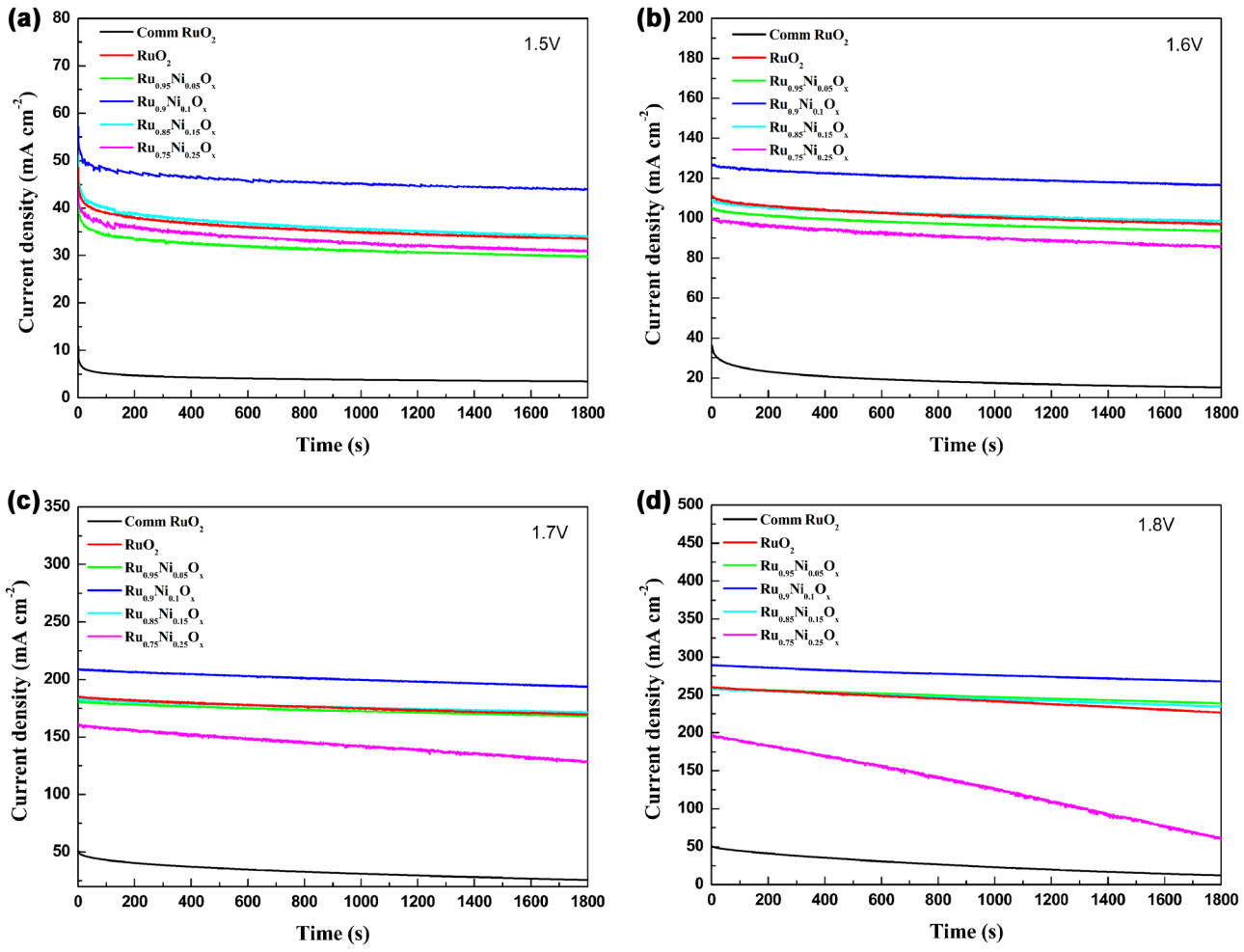

Fig. 9 Chronoamperometry curves of the commercial RuO_2, in-house RuO_2, and $Ru_{1-x}Ni_xO_x$ catalysts performed at (**a**) 1.5 V, (**b**) 1.6 V, (**c**) 1.7 V and (**d**) 1.8 V vs. the RHE in 0.5 M H_2SO_4 at 25 °C and atmospheric pressure

potentials investigated. A similar activity decrease, as was observed in the LSV analysis, was observed when 5 mol% Ni was added to RuO_2, i.e., a slight decrease in activity was observed at potentials 1.5 and 1.6 V. At higher potentials (1.7 and 1.8 V) the activities became similar. The stability of the in-house RuO_2 and $Ru_xNi_{1-x}O_x$ catalysts with up to 20 mol% Ni substitution remained fairly stable over all potentials. Stability for $Ru_{0.75}Ni_{0.25}O_x$ decreased notably at potentials of 1.7 V and 1.8 V. It should be noted that the CA analysis was only performed over an overall duration of 2 h which may account for the differences in stabilities as compared to the CP analysis. The results from CA analysis are consistent with the results from LSV and CP, i.e., when the Ru component is substituted with 10 mol% Ni, there is an improvement in OER activity compared to unsubstituted RuO_2.

Conclusion

Single and binary metal oxides based on Ru and Ni were synthesized, characterized, and evaluated as catalyst materials for the OER in acidic media. Physical characterizations revealed that the Adams fusion method directly produced nano-sized Ru and Ni based oxides. The results indicated that the in-house Ru-based oxides exhibited improved OER performance compared to the commercial RuO_2, under the test conditions. The improved performance of the in-house RuO_2 could be attributable to the synthesis method that produced a RuO_2 catalyst with a larger surface area and smaller crystallite size than the commercial RuO_2 catalyst. XRD analysis revealed that the addition of NiO to RuO_2 induced a phase transformation from a rutile type oxide to an amorphous phase. Electrochemical analyses showed that as expected, NiO was a very poor catalyst for the OER in acidic media however its addition to RuO_2 up to 10 mol%, resulted in enhanced activity and stability of the Ru based catalyst. $Ru_{0.9}Ni_{0.1}O_x$ exhibited a lower overpotential of 0.189 V at 10 $mAcm^{-2}$ compared to the 0.252 V and 0.193 V of the commercial RuO_2 and in-house RuO_2 catalysts, respectively. The commercial RuO_2 catalyst remained stable for only 7 h and the in-house RuO_2 catalyst for 49 h, whereas $Ru_{0.9}Ni_{0.1}O_x$ remained stable until the experimental time limit of 110 h was reached. The improvement in stability was ascribed to NiO acting as the sacrificial material during the OER and thus the addition of the Ni component appears to improve the dispersion of the RuO_2 active sites thereby increasing the available active surface area. However, considering that Ru cost is about 500 times more than that of Ni, the substitution of Ru with Ni by 10 mol%, should help reduce the high cost associated with the OER catalyst.

Acknowledgements This work is funded by the Technology and Human Resources for Industry Program (THRIP/19/31/08/2018) under the Department of Trade, Industry and Competition of the Republic of South Africa. We would also like to thank Isondo Precious Metals as the industrial partner on this THRIP project.

Data Availability The datasets are available from the corresponding author on reasonable request.

Declarations

Conflict of Interest The authors declare no competing interests.

References

1. P.M. Falcone, M. Hiete, A. Sapio, Curr. Opin. Green Sustain. Chem. (2021). https://doi.org/10.1016/j.cogsc.2021.100506
2. T. Bennich, S. Belyazid, I. Stjernquist, A. Diemer, S. Seifollahi-Aghmiuni, Z. Kalantari, J. Clean. Prod. (2021). https://doi.org/10.1016/j.jclepro.2020.125174
3. A.M. Oliveira, R.R. Beswick, Y. Yan, Curr. Opin. Chem. Eng. (2021). https://doi.org/10.1016/j.coche.2021.100701
4. M. Yu, K. Wang, H. Vredenburg, Int. J. Hydrog. Energy. (2021). https://doi.org/10.1016/j.ijhydene.2021.04.016
5. A. Mohammadi, M. Mehrpooya, Energy (2018). https://doi.org/10.1016/j.energy.2018.06.073
6. H. Yu, N. Danilovic, Y. Wang, W. Willis, A. Poozhikunnath, L. Bonville, C. Capuano, K. Ayers, R. Maric, Appl. Catal. B: Environ. (2018). https://doi.org/10.1016/j.apcatb.2018.07.064
7. V. Vij, S. Sultan, A.M. Harzandi, A. Meena, J.N. Tiwari, W.-G. Lee, T. Yoon, K.S. Kim, ACS Catal. (2017). https://doi.org/10.1021/acscatal.7b01800
8. J. Yu, Y. Dai, Q. He, D. Zhao, Z. Shao, M. Ni, Materials Reports. Energy (2021). https://doi.org/10.1016/j.matre.2021.100024
9. Y. Tian, S. Wang, E. Velasco, Y. Yang, L. Cao, L. Zhang, X. Li, Y. Lin, Q Zhang, L. Chen, iScience. (2020). https://doi.org/10.1016/j.isci.2019.100756
10. M. Carmo, D.L. Fritz, J. Mergel, D. Stolten, Int. J. Hydrog. Energy. (2013). https://doi.org/10.1016/j.ijhydene.2013.01.151
11. V. Natarajan, S. Basu, K. Scott, Int. J. Hydrog. Energy. (2013). https://doi.org/10.1016/j.ijhydene.2013.05.133
12. S. Laha, Y. Lee, F. Podjaski, D. Weber, V. Duppel, L.M. Schoop, F. Pielnhofer, C. Scheurer, K. Müller, U. Starke, K. Reuter. B.V. Lotsch, Adv. Energy Mater. (2019). https://doi.org/10.1002/aenm.201803795
13. A. Devadas, S. Baranton, T.W. Napporn, C. Coutanceau, J. Power Sources. (2011). https://doi.org/10.1016/j.jpowsour.2010.11.149
14. S.W. Lee, C. Baik, C. Pak, Catal. Today. (2020). https://doi.org/10.1016/j.cattod.2019.12.003
15. W. Wang, T. Yuan, H. Tang, Z. Hu, Y. Wang, Q. Liu, Chem. Phys. Lett. (2021). https://doi.org/10.1016/j.cplett.2021.138879
16. A. Devadas, S. Baranton, C. Coutanceau, Energy Res. (2020). https://doi.org/10.3389/fenrg.2020.571704
17. M. Tariq, Y. Wu, C. Ma, M. Ali, W.Q. Zaman, Z. Abbas, K.S. Ayub, J. Zhou, G. Wang, L.-M. Cao, J. Yang, Int. J. Hydrog. Energy. (2020). https://doi.org/10.1016/j.ijhydene.2020.04.101
18. L. Qiu, G. Zheng, Y. He, L. Lei, X. Zhang, Chem. Eng. J. (2021). https://doi.org/10.1016/j.cej.2020.128155
19. Z. Ma, Y. Zhang, S. Liu, W. Xu, L. Wu, Y.-C. Hsieh, P. Liu, Y. Zhu, K. Sasaki, J.N. Renner, K.E. Ayers, R.R. Adzic, J.X. Wang, J. Electroanal. Chem. (2018). https://doi.org/10.1016/j.jelechem.2017.10.062

20. Y. Lin, Z. Tian, L. Zhang, J. Ma, Z. Jiang, B.J. Deibert, R. Ge, L. Chen, Nat. Commun. (2019). https://doi.org/10.1038/s41467-018-08144-3
21. J. Yi, W.H Lee, C.H. Choi, Y. Lee, K.S. Park, B.K. Min, Y.J. Hwang, H-S. Oh, Electrochem. Commun. (2019). https://doi.org/10.1016/j.elecom.2019.05.018
22. G. Lin, Y. Wang, J. Hong, K. Suenaga, L. Liu, L.-Y. Chang, C.-W. Pao, T. Zhang, W. Zhao, F. Huang, M. Yang, Y.-Y. Sun, J. Wang, Chemsuschem (2020). https://doi.org/10.1002/cssc.202000213
23. S. Shiva Kumar, S.U.B. Ramakrishna, D. Bhagawan, V. Himabindu, Ionics. (2018). https://doi.org/10.1007/s11581-017-2359-4
24. N. Li, T.P. Keane, S.S Veroneau, R.G. Hadt, D. Hayes, L.X. Chen, D.G. Nocera, Proc. Natl. Acad. Sci. (2020). https://doi.org/10.1073/pnas.2001529117
25. J. Cheng, H. Zhang, H. Ma, H. Zhong, Y. Zou, Int. J. Hydrog. Energy. (2009). https://doi.org/10.1016/j.ijhydene.2009.06.061
26. S. Chalupczok, P. Kurzweil, H. Hartmann, C. Schell, Int. J. Electrochem. Sci. (2018). https://doi.org/10.1155/2018/1273768X-K
27. K. Juodkazis, J. Juodkazytė, R. Vilkauskaite, B. Šebeka, V. Jasulaitiene, Chemija **19**, 1 (2008)
28. Gu, J.C.A. Camayang, E. Samira, E. Nikolla, J. Catal. (2020). https://doi.org/10.1016/j.jcat.2020.05.008

Publisher's Note Springer Nature remains neutral with regard to jurisdictional claims in published maps and institutional affiliations.

Springer Nature or its licensor (e.g. a society or other partner) holds exclusive rights to this article under a publishing agreement with the author(s) or other rightsholder(s); author self-archiving of the accepted manuscript version of this article is solely governed by the terms of such publishing agreement and applicable law.